

Doppler Spectra of Microwave Scattering Fields From Nonlinear Oceanic Surface at Moderate- and Low-Grazing Angles

Yunhua Wang, Yanmin Zhang, Mingxia He, and Chaofang Zhao

Abstract—Results of microwave radar Doppler spectra from 1-D nonlinear ocean surface at moderate- and low-grazing angles are calculated by the composite surface scattering model. For the large-scale undulating surface description, the narrow-band Lagrange model is used, which takes into account the vertical and horizontal skewnesses. Moreover, the shadow and the curvature effects of large-scale waves on the Doppler spectra are also considered in our calculations. Comparisons of computed curves with experimentally measured Doppler spectra at different incidence angles and at various wind speeds show that the simulated results can fit the measured data well at moderate incident angles. From the simulations, we also find that the hydrodynamic modulation and the horizontal skewness of the large-scale waves can induce remarkable influence on Doppler shift. In addition, when the shadow and the curvature effects of large-scale waves are considered in the calculations, the Doppler shifts grow more quickly and the spectral widths become narrower at low-grazing angles, and this is consistent with the numerical results given by Toporkov *et al.* in the nonlinear surface case. The conclusions obtained in this work seem promising for better understanding the properties of time-dependent radar echoes from oceanic surfaces.

Index Terms—Doppler spectra, Lagrange sea surface, scattering.

I. INTRODUCTION

DOPPLER spectra of electromagnetic signals backscattered from time-varying oceanic surfaces have attracted much attention, experimentally as well as theoretically [1]–[13]. This issue is of practical importance in areas of sea surface wind retrieving, sea wave monitoring, and oceanic surface current measuring [14]–[19]. Among the analytical efforts, the early works of Crombie [1], Barrick [2], Bass *et al.* [3], and Wright and Keller [4] should be mentioned. For HF

waves, Crombie [1] explained the Doppler spectrum using the Bragg scattering mechanism. Barrick [2] developed a perturbative model based on a representation of sea waves up to the second order. The Doppler model given by Barrick *et al.* has been extensively used with success under various situations for HF and VHF radars. For microwaves, Bass *et al.* [3] and Wright and Keller [4] proposed a composite (two-scale) surface scattering model which includes the modulation of the wavelets by the long waves. This composite surface scattering model can explain the polarization dependence of the echo and yield decent approximations of its intensity and Doppler bandwidth. So far, the composite surface model is still a practical tool for the theoretical description of the Doppler spectrum of microwave scattering from time-varying sea surface. More recently, for the case of moderate- and low-grazing angles, Doppler spectra calculations based on the composite surface model and a comparison with experimental data were reported in [5]. However, it should be pointed out that the time-varying sea surface model utilized in [5] is a linear superposition of free waves with random phases. Nevertheless, it is now well established that the effects of the surface nonlinearities, such as the horizontal skewness, cannot be neglected if one aims at interpreting the Doppler spectra of backscattered fields [6], [7]. In the framework of the composite surface model, Doppler shift of radar backscattering from nonlinear Gerstner's wave was considered by Fuks and Voronovich [8]. Unfortunately, the conventional Gerstner's surface model which has a pure trochoidal shape cannot represent the geometrical structure of a random sea surface well.

In recent years, based on the exact numerical methods, some relevant investigations on Doppler spectra of backscattering from linear and nonlinear surfaces were reported [9]–[11]. In [9], using the method of moment, Doppler spectra were simulated with nonlinear surfaces proposed by Creamer *et al.* [20]. The numerical simulations performed by Toporkov *et al.* show an obvious broadening of the bandwidth for nonlinear surfaces at low-grazing angles (LGAs) and a separation of the vertical and horizontal polarization spectra at LGAs for nonlinear surfaces. However, this spectral separation at LGAs cannot be observed for the linear sea surface. In [10] and [11], Johnson *et al.* and Hayslip *et al.* further investigated the influences of the hydrodynamic models on the Doppler spectra of L-band backscattered fields. In spite of the advantages, several questions should be mentioned as follows. First, using exact numerical methods, Doppler simulations turn out to be

Manuscript received June 5, 2010; revised November 12, 2010, February 7, 2011, June 3, 2011, and July 24, 2011; accepted August 7, 2011. Date of publication October 21, 2011; date of current version March 28, 2012. This work was supported in part by the Young Scientists Fund of the National Natural Science Foundation of China under Grant 40906088, by the Specialized Research Fund for the Doctoral Program of Higher Education under Grant 200804231021, and by the Fundamental Research Fund for the Central Universities under Grant 201013028.

Y. Wang, M. He, and C. Zhao are with the Ocean Remote Sensing Institute, Ocean University of China, Qingdao 266003, China (e-mail: wyh78917@yahoo.com.cn; mxhe@orsi.ouc.edu.cn; zhao cf@ouc.edu.cn).

Y. Zhang is with the College of Information Science and Engineering, Ocean University of China, Qingdao 266100, China (e-mail: zhangyanmin79@163.com).

Color versions of one or more of the figures in this paper are available online at <http://ieeexplore.ieee.org>.

Digital Object Identifier 10.1109/TGRS.2011.2164926

quite computationally expensive; second, influences of different factors, such as hydrodynamic modulation, tilt modulation, shadow effect of long waves, and so on, cannot be considered individually.

In this paper, Doppler spectra from nonlinear oceanic surface at microwave bands are presented by the two-scale scattering model, and choosing this scattering model is mainly due to two reasons: 1) We attempt to analyze the effects of different factors, such as the shadow, the curvature, the hydrodynamic modulation, etc., on Doppler behaviors individually, and 2) the two-scale scattering model is an approximation method, so its computational load is much less than that of the numerical methods. It is well known that the simulation of the Doppler spectrum from the ocean surface requires accurate descriptions of the sea surface slope and the sea surface motion. One of the main difficulties lies in the fact that the geometry of the sea surface is of complex characteristic, involving the randomness and nonlinear wave interactions. In Section II, the narrow-band Lagrange model is introduced to simulate the nonlinear sea surface, in which the vertical and horizontal skewnesses are both considered [21], [22]. In Section III, we suppose that the 1-D ocean gravity waves can be described by a spectrum with a $|K|^{-3}$ dependence, and then, the hydrodynamic modulation function of small-scale ripples by long waves is derived using the weak hydrodynamic interaction theory [23]–[25]. In Section IV, a Doppler spectrum model for backscattering field is proposed. In our Doppler spectrum model, the shadow and curvature effects of large-scale waves are also taken into account. Section V is devoted to the results and the comments while the concluding remarks and perspectives are provided in Section VI.

II. NONLINEAR GRAVITY WAVES

In this paper, we will concentrate on the problem of 1-D surface for no appropriate hydrodynamic model can be used to simulate 2-D front-tilted waves. Nevertheless, the extension to the 2-D case does not raise any particular problem except the 2-D hydrodynamic wave model.

In accordance with the linear theory, the irregular sea surface is described as a sum of harmonics with different amplitudes, frequencies, and random phases. The motion of such a deterministic sample can be easily derived from the dispersion relation or from the scalar velocity potential function. However, if one aims at interpreting radar Doppler spectra, the nonlinearities of the actual sea surface cannot be neglected. In the usual manner, the profile of the 1-D nonlinear sea surface can be expanded in perturbation series. The first-order perturbation term corresponds to the linear surface and the higher order corrections come from the expansion of the hydrodynamic formulas in terms of wave interactions. With the narrow-band assumption, Tayfun [26] suggested a perturbation model including a second-order expansion term. The nonlinear part obtained by Tayfun's model results in a random sea surface with narrow and peaked crests and long and flat troughs. Such an asymmetry in the vertical direction is referred to as vertical skewness. On the other hand, horizontal skewness, which directly affects the surface slope distribution, can also occur in deep water sea waves.

However, the nonlinear models mentioned earlier cannot include any asymmetry due to tilted crests in the horizontal direction. Just as Fung and Chen *et al.* pointed out [27], [28], compared with vertical skewness, horizontal skewness induces more remarkable influence on backscattered signals because the latter is a result of deformations in the surface slopes. Then, Fung and Chen *et al.* modified Tayfun's model for nonlinear gravity waves to accommodate both vertical and horizontal skewnesses [27], [28]. The Lagrange model with linked components (hereinafter referred to as LMLC) is also an optional hydrodynamic model for the nonlinear stochastic water waves. Recent studies by Lindgren and Aberg [21], [22] have shown that the LMLC can simulate realistic vertical and horizontal skewnesses. For deepwater waves, the LMLC can be written as

$$z(x, t) = \sum_{i=1}^N A_i \cos(K_i x_0 - \omega_i t + \varphi_i) \quad (1)$$

$$x = x_0 - \sum_{i=1}^N A_i \sin(K_i x_0 - \omega_i t + \varphi_i) + \sum_{i=1}^N \alpha_i A_i \cos(K_i x_0 - \omega_i t + \varphi_i) \quad (2)$$

with

$$A_i = \sqrt{W(K_i) [Rn_{ri}(0, 1)^2 + Rn_{si}(0, 1)^2] \Delta K} \quad (3)$$

where x_0 is the abscissa of the water particle's equilibrium position. The wavenumber separation ΔK is related to the length L of the surface by $\Delta K = 2\pi/L$. Moreover, the spatial wavenumber $K_i = i\Delta K$, and the angular frequency $\omega_i = \sqrt{gK_i}$, in which g denotes the gravity acceleration constant. $W(K)$ is the isotropic part of the spectrum proposed by Elfouhaily *et al.* [29]. φ_i represents a random phase uniformly distributed over the interval $(0, 2\pi)$. The linking parameter can be written as $\alpha_i = \gamma/\omega_i^2$, and γ can be determined by the relation between the horizontal acceleration of water particles and vertical displacement [21], [22]. In (3), $Rn_{ri}(0, 1)$ and $Rn_{si}(0, 1)$ are independent Gaussian random numbers with zero mean and unit variance. Substituting (2) into (1), we obtain

$$\begin{aligned} z(x, t) &\approx \sum_{i=1}^N A_i \cos \left[K_i x - \omega_i t + \varphi_i \right. \\ &\quad \left. + K_i \sum_{j=1}^N A_j \sin(K_j x - \omega_j t + \varphi_j) \right. \\ &\quad \left. - K_i \sum_{j=1}^N \alpha_j A_j \sin(K_j x - \omega_j t + \varphi_j) \right] \\ &\approx \sum_{i=1}^N A_i \cos(K_i x - \omega_i t + \varphi_i) \\ &\quad - \sum_{i=1}^N \sum_{j=1}^N K_i A_i A_j \sin(K_i x - \omega_i t + \varphi_i) \end{aligned}$$

$$\begin{aligned}
& \times \sin(K_j x - \omega_j t + \varphi_j) \\
& + \sum_{i=1}^N \sum_{j=1}^N \alpha_j K_i A_i A_j \sin(K_i x - \omega_i t + \varphi_i) \\
& \times \cos(K_j x - \omega_j t + \varphi_j) \\
& = \sum_{i=1}^N A_i \cos(K_i x - \omega_i t + \varphi_i) \\
& + \frac{1}{2} \sum_{i=1}^N \sum_{j=1}^N K_i A_i A_j \\
& \times \cos[(K_i + K_j)x - (\omega_i + \omega_j)t + \varphi_i + \varphi_j] \\
& + \frac{1}{2} \sum_{i=1}^N \sum_{j=1}^N K_i A_i A_j \\
& \times \cos[(K_i - K_j)x - (\omega_i - \omega_j)t + \varphi_i - \varphi_j] \\
& + \frac{1}{2} \sum_{i=1}^N \sum_{j=1}^N \alpha_j K_i A_i A_j \\
& \times \sin[(K_i + K_j)x - (\omega_i + \omega_j)t + \varphi_i + \varphi_j]. \quad (4)
\end{aligned}$$

Supposing that gravity waves satisfy the narrow-band assumption, a narrow-band representation for $z(x, t)$ is provided in the form

$$\begin{aligned}
z(x, t) &= \sum_{i=1}^N A_i \cos(K_i x - \omega_i t + \varphi_i) \\
& + \frac{\tilde{K}}{2} \sum_{i=1}^N \sum_{j=1}^N A_i A_j \\
& \times \cos[(K_i + K_j)x - (\omega_i + \omega_j)t + \varphi_i + \varphi_j] \\
& + \frac{\tilde{K}}{2} \sum_{i=1}^N \sum_{j=1}^N \alpha_j A_i A_j \\
& \times \sin[(K_i + K_j)x - (\omega_i + \omega_j)t + \varphi_i + \varphi_j] \\
& = \sum_{i=1}^N A_i \cos(K_i x - \omega_i t + \varphi_i) + \frac{\tilde{K}}{2} \sum_{i=1}^N \sum_{j=1}^N P A_i A_j \\
& \times \cos[(K_i + K_j)x - (\omega_i + \omega_j)t + \varphi_i + \varphi_j - \beta_j] \quad (5)
\end{aligned}$$

where the parameter $P = \sqrt{1 + \alpha_j^2}$

$$\beta_j = \arctan(\alpha_j) = \arctan(\gamma/\omega_j^2) \quad (6)$$

and the average wavenumber \tilde{K} is defined as

$$\tilde{K} = \frac{\int_0^{K_{\max}} K W(K) dK}{\int_0^{K_{\max}} W(K) dK} \quad (7)$$

with $K_{\max} = N\Delta K$.

For narrow-band waves, β_j can be considered as the biphas defined in [30] and [31], and $\gamma = 0$ (i.e., $\beta_j = 0$) and $\gamma = \omega_j^2$

(i.e., $\beta_j = \pi/4$) correspond to nonlinear sea surface models proposed in [26] and in [27] and [28], respectively. In [21] and [22], Lindgren and Aberg set $\gamma = 0.4$ or 0.8 for horizontal skewness water waves. However, strong correlation between biphas β_j and wind forcing was found by Leykin *et al.* through experiments in a laboratory wave tank under varied wind and fetch conditions [32]. Unfortunately, few data measured from actual sea waves are presently available for direct comparison with the results of Leykin *et al.* In this paper, we set $\gamma = 0.4$. In (5), the nonlinear component of the wave profile contains two terms, i.e., the second and the third term of the first equality, and the vertical and horizontal skewnesses are due to the second and the third term, respectively [33].

In the same way, the horizontal displacement $h(x, t)$ of water particles can be derived as

$$\begin{aligned}
h(x, t) &= - \sum_{i=1}^N A_i \sin(K_i x - \omega_i t + \varphi_i) \\
& + \sum_{i=1}^N \alpha_i A_i \cos(K_i x - \omega_i t + \varphi_i) \\
& + \tilde{K} \sum_{i=1}^N \sum_{j=1}^N \alpha_i A_i A_j \\
& \times \cos[(K_i + K_j)x - (\omega_i + \omega_j)t + \varphi_i + \varphi_j] \\
& - \frac{\tilde{K}}{2} \sum_{i=1}^N \sum_{j=1}^N A_i A_j \\
& \times \sin[(K_i + K_j)x - (\omega_i + \omega_j)t + \varphi_i + \varphi_j] \\
& + \frac{\tilde{K}}{2} \sum_{i=1}^N \sum_{j=1}^N \alpha_i \alpha_j A_i A_j \\
& \times \sin[(K_i + K_j)x - (\omega_i + \omega_j)t + \varphi_i + \varphi_j]. \quad (8)
\end{aligned}$$

Supposing that the orbit velocity field of a particle on the nonlinear sea surface is denoted by $(V_v(x, t), V_h(x, t))$, the vertical and horizontal components of the orbit velocity can be deduced by the derivative of (5) and (8) with respect to t as follows:

$$\begin{aligned}
V_v(x, t) &= \sum_{i=1}^N \omega_i A_i \sin(K_i x - \omega_i t + \varphi_i) \\
& + \frac{\tilde{K}}{2} \sum_{i=1}^N \sum_{j=1}^N (\omega_i + \omega_j) A_i A_j \\
& \times \sin[(K_i + K_j)x - (\omega_i + \omega_j)t + \varphi_i + \varphi_j] \\
& - \frac{\tilde{K}}{2} \sum_{i=1}^N \sum_{j=1}^N (\omega_i + \omega_j) \alpha_j A_i A_j \\
& \times \cos[(K_i + K_j)x - (\omega_i + \omega_j)t + \varphi_i + \varphi_j] \quad (9) \\
V_h(x, t) &= \sum_{i=1}^N \omega_i A_i \cos(K_i x - \omega_i t + \varphi_i) \\
& + \sum_{i=1}^N \omega_i \alpha_i A_i \sin(K_i x - \omega_i t + \varphi_i)
\end{aligned}$$

$$\begin{aligned}
& + \tilde{K} \sum_{i=1}^N \sum_{j=1}^N (\omega_i + \omega_j) \alpha_i A_i A_j \\
& \times \sin [(K_i + K_j)x - (\omega_i + \omega_j)t + \varphi_i + \varphi_j] \\
& + \frac{\tilde{K}}{2} \sum_{i=1}^N \sum_{j=1}^N (\omega_i + \omega_j) A_i A_j \\
& \times \cos [(K_i + K_j)x - (\omega_i + \omega_j)t + \varphi_i + \varphi_j] \\
& - \frac{\tilde{K}}{2} \sum_{i=1}^N \sum_{j=1}^N (\omega_i + \omega_j) \alpha_i \alpha_j A_i A_j \\
& \times \cos [(K_i + K_j)x - (\omega_i + \omega_j)t + \varphi_i + \varphi_j]. \quad (10)
\end{aligned}$$

III. HYDRODYNAMIC MODULATION

It is well known that the Bragg scattering field from sea surface is affected not only by the tilt modulation but also by the hydrodynamic modulation. Unfortunately, up to now, the hydrodynamic modulation transfer function R^{hydr} is less well known. Based on the weak hydrodynamic interaction theory, a theoretical value for R^{hydr} was derived in [23] and [24]. However, it is questionable whether this R^{hydr} value is realistic because wind-induced straining is not considered [25]. Since the hydrodynamic modulation function of small-scale ripples by nonlinear long waves is still under investigation so far, the R^{hydr} developed in [25] is employed in this paper

$$R^{hydr} = -\frac{\omega - j\mu}{\omega^2 + \mu^2} \frac{\omega}{|\mathbf{K}|} (\mathbf{K} \cdot \mathbf{K}_s) \left[\frac{1}{W_s} \mathbf{K} \cdot \frac{\partial W_s}{\partial \mathbf{K}_s} - \frac{1}{2} \frac{\mathbf{K} \cdot \mathbf{K}_s}{|\mathbf{K}_s|^2} \right] \quad (11)$$

where \mathbf{K} and \mathbf{K}_s denote the wavenumber of the large- and small-scale waves, respectively. W_s denotes the roughness spectrum of short waves which are not modulated by large-scale waves. μ is the relaxation rate and has to be determined by experiments. However, the relaxation rate is poorly known experimentally. Moreover, the values estimated by various investigators differ by almost one order of magnitude [34]. Here, we take the following values for μ as reference values: For wind speeds ≥ 7 m/s, $\mu = 0.1$ s⁻¹ for L-band radar wave, and $\mu = 1.7$ s⁻¹ for X- and Ku-band radar waves; for low wind speeds, $\mu = 0.01$ s⁻¹ for L-band radar wave, and $\mu = 0.24$ s⁻¹ for X- and Ku-band radar waves.

If we suppose that the 1-D small-scale waves can be described by a roughness spectrum with a $|K|^{-3}$ dependence, the hydrodynamic modulation function R^{hydr} takes a simple form

$$R^{hydr}(K) = 3.5 |K| \omega \frac{\omega - j\mu}{\omega^2 + \mu^2}. \quad (12)$$

Then, the roughness spectrum of the short waves modulated by the large-scale waves can be obtained as

$$W_{ms}(K, x, t) = W_s + \frac{W_s}{2\pi} \int R^{hydr}(K') \cdot \Gamma(K') \exp(jK'x - j\omega't) dK' \quad (13)$$

where $\Gamma(K')$ denotes the Fourier transform of the surface elevation $z_l(x, t)$ associated with large-scale waves. W_s and $z_l(x, t)$ will be given definitely in the following section.

IV. DOPPLER SPECTRUM IN A TWO-SCALE MODEL

In this section, based on the two-scale scattering model, we proposed a Doppler spectrum model in which the shadow and curvature effects of the large-scale waves are considered. In the general framework of the two-scale scattering model, the composite sea surface roughness $\eta(x, t)$ is rearranged into the following form:

$$\eta(x, t) = z_l(x, t) + z_s(x, t) \quad (14)$$

where $z_l(x, t)$ denotes the large-scale component which supposedly acts as a smooth facet and $z_l(x, t)$ is generated by the LMLC. $z_s(x, t)$ represents a small-scale roughness superimposed on the large-scale one and statistically independent at different facets. The spectrum for $z_l(x, t)$ is $W_l(K) = \begin{cases} W(K) & \text{for } K \leq K_C \\ 0 & \text{for } K > K_C \end{cases}$, while the spectrum for $z_s(x, t)$ is $W_s(K) = \begin{cases} 0 & \text{for } K \leq K_C \\ W(K) & \text{for } K > K_C \end{cases}$. The cutoff wavenumber K_C can range from $K_{Bragg}/6$ to $K_{Bragg}/3$ [35], and here, we choose the latter value. $K_{Bragg}(\theta_i) = 2k_i \sin \theta_i$ is the Bragg wavenumber.

For 1-D rough surface, the formula in the conventional two-scale scattering model can be simplified as [36]

$$\sigma_{pp}(\theta_i) = \int_{-\infty}^{\infty} \sigma_{pp}^s(\theta'_i) P(z_x) dz_x \quad (15)$$

where θ'_i denotes the incident angle in the local reference frame. $P(z_x)$ is the probability density function (pdf) of the large-scale wave slope. $\sigma_{pp}^s(\theta'_i)$ denotes the first-order backscattering coefficient from the small-scale waves for the pp (HH or VV) polarization. For the case of 1-D surface, it can be written as

$$\sigma_{pp}^s(\theta'_i) = 4k_i^3 \cos^4 \theta'_i |\alpha_{pp}| W_s(2k_i \sin \theta'_i) \quad (16)$$

where

$$\alpha_{pp} = \begin{cases} \frac{\varepsilon_r - 1}{[\cos \theta'_i + \sqrt{\varepsilon_r - \sin^2 \theta'_i}]^2} & \text{for HH-pol} \\ \frac{(\varepsilon_r - 1)[\varepsilon_r(1 + \sin^2 \theta'_i) - \sin^2 \theta'_i]}{[\varepsilon_r \cos \theta'_i + \sqrt{\varepsilon_r - \sin^2 \theta'_i}]^2} & \text{for VV-pol} \end{cases} \quad (17)$$

and $k_i = 2\pi/\lambda$ is the wavenumber of the incident field.

At LGAs, the large-scale component of sea surface should be considered as curved surface. Just as Voronovich pointed out in [35] and [37], the influences of curvature on backscattered echoes should be taken into account. Here, the backscattering coefficient $\sigma_{pp}^s(\theta')$ is modified by the factor given by Voronovich and Zavorotny [35]

$$\sigma_{ppc}^s(\theta'_i) = \sigma_{pp}^s(\theta'_i) C_{pp}(\theta'_i, r_x) \quad (18)$$

where the modified factor of curvature in (18) is

$$C_{pp}(\theta'_i, r_x) = \begin{cases} \frac{|\sqrt{\varepsilon_2 - \varepsilon_1} \sin^2 \theta_i + \sqrt{\varepsilon_1} \cos \theta_i|^4}{|\sqrt{\varepsilon_2 - \varepsilon_1} \sin^2 \theta_i a^* + \sqrt{\varepsilon_1} \cos \theta_i b^*|^4} & \text{for HH-Pol} \\ \frac{|\varepsilon_1 \sqrt{\varepsilon_2 - \varepsilon_1} \sin^2 \theta_i + \varepsilon_2 \sqrt{\varepsilon_1} \cos \theta_i|^4}{|\varepsilon_1 \sqrt{\varepsilon_2 - \varepsilon_1} \sin^2 \theta_i a^* + \varepsilon_2 \sqrt{\varepsilon_1} \cos \theta_i b^*|^4} & \text{for VV-Pol} \end{cases} \quad (19)$$

with

$$r_x(x, t) = \frac{(1 + z_l'^2)^{3/2}}{|z_l''|} \quad (20)$$

$$a = \sqrt{\frac{\pi\tau}{2}} H_{1/3}^{(1)}(\tau) \exp\left(-j\tau + j\frac{5\pi}{12}\right) \quad (21)$$

$$b = -\frac{j}{3 \sin^2 \theta_i} \sqrt{\frac{\pi}{2\tau}} \left[(1 - 3j\tau \cos^2 \theta_i) H_{1/3}^{(1)}(\tau) + 3t H_{1/3}^{(1)'}(\tau) \right] \times \exp\left(-j\tau + j\frac{5\pi}{12}\right) \quad (22)$$

$$\tau = \frac{1}{3} k_i \sqrt{\varepsilon_1} r_x \frac{\cos^3 \theta_i}{\sin^2 \theta_i}. \quad (23)$$

z_l' and z_l'' denote the first- and second-order derivatives of the large-scale surface with respect to x , $H_{1/3}^{(1)}(\tau)$ is the 1/3 order Hankel function of the first kind, and ε_1 and ε_2 denote the permittivities of air and sea water, respectively.

On the other hand, when the incidence angle is large, some facets of the sea surface cannot be illuminated by the incident wave due to the shadowing of others. Here, in order to take into account the possible partial shadowing of the large-scale surface, a shadow function $S(\theta_i, x)$ will be introduced into (18). In this paper, the ray tracing method is used to calculate the shadow function for arbitrary incident angles. First, we define the projection line, which is perpendicular to the incident direction, as

$$z = \tan \theta_i x. \quad (24)$$

For each facet, we first determine whether its projection on the projection line has area in common with the others. If so, the facet will not be illuminated and the shadow function $S(\theta_i, x) = 0$; otherwise, the facet is illuminated by the incident field, and the shadow function $S(\theta_i, x) = 1$.

If the effects of curvature, shadow, and hydrodynamic modulation are all considered, (18) can be modified as

$$\sigma_{pp}^m(\theta'_i, x, t) = 4k_i^3 \cos^4 \theta'_i |\alpha_{pp}| W_{ms} \times (2k_i \sin \theta'_i, x, t) C_{pp}(\theta'_i, R_x) S(\theta_i, x) \quad (25)$$

where $W_{ms}(2k_i \sin \theta'_i, x, t)$ is the spectrum of the Bragg resonant waves modulated by large-scale waves.

If we regard sea surface as a stationary ergodic process, using $\sigma_{pp}^m(\theta'_i, x, t)$ instead of $\sigma_{pp}^s(\theta'_i)$ and replacing the integration in (15) by a summation, we obtain the mean scattering coefficient $\sigma_{pp}(\theta_i)$ as

$$\sigma_{pp}(\theta_i) = \frac{1}{N} \sum_{n=1}^N \sigma_{pp}^m(\theta'_i, x_n, t) \quad (26)$$

where N denotes the number of scattering facets on large-scale waves.

Assuming that Doppler shift f_{Dpp} is a simple arithmetic mean weighted by the scattering coefficient of each surface facet, it is defined as

$$f_{Dpp} = \frac{\langle f \sigma_{pp}^m \rangle}{\langle \sigma_{pp}^m \rangle} + f_{Bragg} + f_{drift} \quad (27)$$

where the Bragg frequency f_{Bragg} is

$$f_{Bragg} = \frac{1}{2\pi} \sqrt{g K_{Bragg}(\theta_i)} \quad (28)$$

and $f_{drift} = k_i U_{drift} / \pi$, $U_{drift} \approx 0.03 U_{10}$, U_{10} is the wind speed at a height of 10 m [38].

Using (9), (10), (26), and (27), it is obtained that

$$f_{Dpp} = \frac{\sum_{n=1}^N \sigma_{pp}^m(\theta'_i, x_n, t) k_i V_p}{\pi N \sigma_{pp}^s} + f_{Bragg} + f_{drift}. \quad (29)$$

Here, $V_p = V_v(x_n, t) \cos \theta_i - V_h(x_n, t) \sin \theta_i$ denotes the line-of-sight velocity of each scattering facet, and the orbit velocity ($V_v(x_n, t), V_h(x_n, t)$) can be evaluated by (9) and (10).

Doppler bandwidth δf , i.e., the second moment of the Doppler spectrum, is defined as [39], [40]

$$\delta f_{pp}^2 = \frac{\langle f^2 \sigma_{pp} \rangle}{\langle \sigma_{pp} \rangle} - \left[\frac{\langle f \sigma_{pp} \rangle}{\langle \sigma_{pp} \rangle} \right]^2 \quad (30)$$

then, we can obtain that

$$\delta f_{pp} = \sqrt{\frac{\sum_{n=1}^N \sigma_{pp}^m(\theta'_i, x_n, t) k_i^2 V_p^2}{N \pi^2 \sigma_{pp}^s} - (f_{Dpp} - f_{Bragg} - f_{drift})^2}. \quad (31)$$

Supposing that the Doppler spectrum has Gaussian shape, using the Doppler shift and the bandwidth given by (29) and (31), we finally obtain the Doppler spectrum models as

$$DS_{Dpp}(f_D) = \frac{\sigma_{pp}(\theta_i)}{\sqrt{2\pi \delta f_{pp}^2}} \exp \left\{ -\frac{(f_D - f_{Dpp})^2}{2\delta f_{pp}^2} \right\}. \quad (32)$$

On the other hand, the Doppler spectrum can also be obtained by numerical simulations directly, i.e.,

$$DS_{DppN}(f_D) = \frac{\sum_{n=1}^N \sigma_{pp}^m(\theta'_i, x_n, t) \cdot \Xi(n)}{N \Delta f} \quad (33)$$

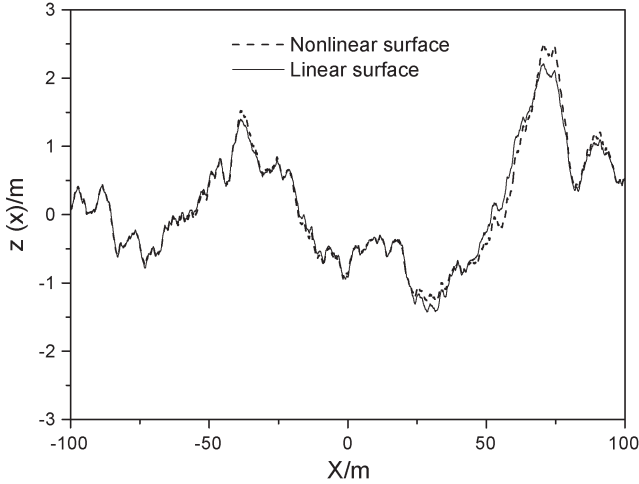


Fig. 1. Comparison of (dashed line) nonlinear LMLC and (solid line) linear surface profiles.

where Δf denotes the separation of the Doppler frequency f_D and

$$\Xi(n) = \begin{cases} 1 & \text{for } f_D \leq f_n < (f_D + \Delta f) \\ 0 & \text{for } f_n < f_D \text{ or } f_n \geq (f_D + \Delta f) \end{cases} \quad (34)$$

with

$$f_n = \left\{ \frac{k_i}{\pi} V_p + f_{Bragg} + f_{drift} \right\}. \quad (35)$$

V. NUMERICAL RESULTS AND DISCUSSIONS

In this section, we start with examining the statistic characteristics of the nonlinear sea surface modified by LMLC. In the simulations, the number of surface samples is $N = 32\,768$, the surface length is $L = 327.68$ m, and the discrete step in the wavenumber domain is $\Delta K = 0.0134$ rad/m. The statistical distributions of the linear and the nonlinear LMLC sea surfaces are all calculated by averaging over 100 realizations.

Fig. 1 illustrates the simulated profiles of nonlinear LMLC surface and linear surface. Here, the wind speed is $U_{10} = 10$ m/s. From Fig. 1, it can be seen that the main differences between nonlinear and linear profiles are in the crests and troughs. The nonlinear sea surface profile has flattened troughs and narrower and larger peaks. In addition, for the nonlinear sea surface profile, the crests tilt in the downwind direction.

Theoretical and experimental analyses show that sea surface elevation and slope can be described by the Gram–Charlier distribution [41]–[43]. Hence, in Figs. 2 and 3, the pdfs of the normalized sea surface elevation and normalized slope are both compared with the Gram–Charlier distribution. Fig. 2 shows the normalized sea surface elevation $\xi = z/\sigma_{sea}$, and σ_{sea} denotes the root mean square of sea surface roughness z . The nonlinear sea surface profile has flattened troughs and narrower peaks; therefore, more points lie below the mean sea surface (taken to be the origin), and the height pdf for nonlinear sea surface is more peaked below the origin. Meanwhile, one also can see that

the height pdf corresponding to the nonlinear LMLC surface fits the Gram–Charlier distribution better.

The normalized slope pdfs of the nonlinear and linear surfaces are compared with the Gram–Charlier distribution proposed by Cox and Munk [42], [43] in Fig. 3. Because the crests of the nonlinear sea surface tilt in the downwind direction and the troughs tilt in the opposite direction, just as shown in the figure, on the nonlinear surface, there should be more points whose slopes are below zero. From the comparisons in Fig. 3, we also find that the slope pdf of the nonlinear LMLC surface can fit the Gram–Charlier distribution better than that corresponding to the linear surface for different wind speeds.

Fig. 4 illustrates the pdf of the vertical component of the orbit velocity. From the comparison between the simulated results and the measured data in a wave tank, it is obvious that the pdf of the nonlinear LMLC sea surface can fit the measurements better. However, it should be pointed out that the pdf of the orbit velocity simulated numerically by the nonlinear LMLC surface should be further verified by the measured data from actual sea waves.

From the aforementioned discussions, we can get an impression that the nonlinear LMLC sea surface model does seem to produce the desired sea surface profile. In Figs. 5 and 6, Doppler spectra of backscattering echoes from time-varying sea surfaces simulated by the nonlinear LMLC model are compared with the experimental data measured at incidence angles between 50° and 80° during the Synthetic Aperture Radar and X-Band Ocean Nonlinearities-Forschungsplattform Nordsee experiment [45]. The series of experimental data were collected from a dual-polarized Ku-band (14-GHz) scatterometer with the antennas directed nearly into the wind (downwind direction). In Figs. 5 and 6, the wind speeds are $U_{47} = 7$ m/s and $U_{47} = 16$ m/s at a height of 47 m above sea surface, respectively. Here, it should be pointed out that the Elfouhaily spectrum used in this paper is parameterized by the wind speed at a height of 10 m above sea surface, i.e., U_{10} . Thus, the wind speeds in Figs. 5 and 6 (i.e., U_{47}) have been recalibrated to U_{10} by the following empirical formula [48]

$$U_{10} = U_h \frac{\ln(10/z_0)}{\ln(h/z_0)} \quad (36)$$

where $z_0 = 3.0 \times 10^{-3}$ m and U_h denotes the wind speed at a height of h above sea surface.

From Figs. 5 and 6, one can find that the Doppler measurements and the simulated results with the nonlinear sea surface agree well except the HH-pol cases at large incidence angles. The Doppler shifts of HH-pol spectra simulated by (33) (dark line) are smaller than measured data when the incident angle is 80° . The possible reason for this phenomenon is that, in our simulations, the contributions of the scattering fields from bound waves, which clearly affect HH-pol results at larger incidence angles, are not taken into account. The bound waves localize on the front faces of large-scale waves in the vicinity of their crests and propagate with a velocity close to the phase velocity of the corresponding large-scale gravity waves. Thus, the Doppler shifts of HH-pol spectra which are

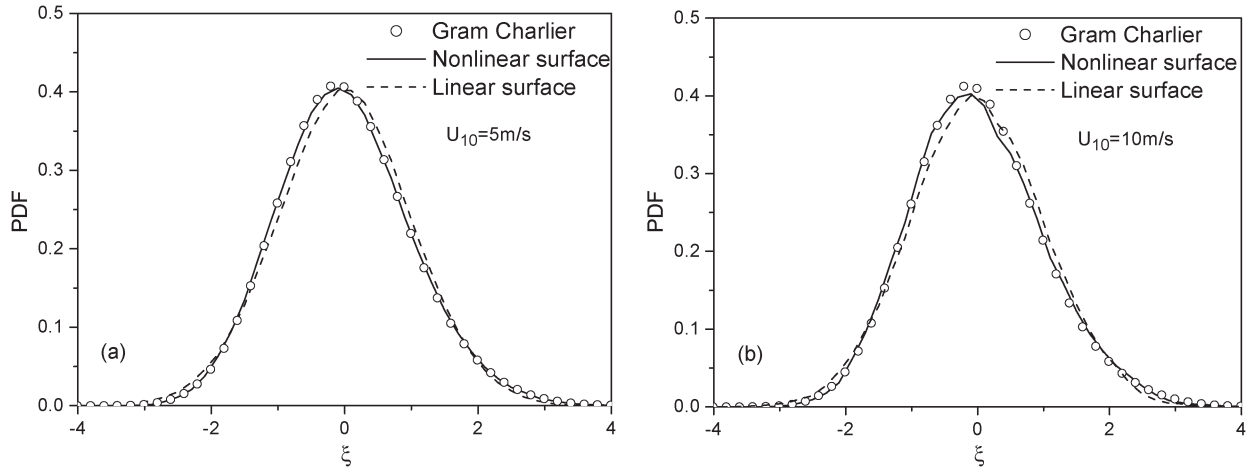


Fig. 2. Comparisons of the surface elevation pdfs among the (dashed line) nonlinear surface, (solid line) linear surface, and (circles) Gram–Charlier distribution.

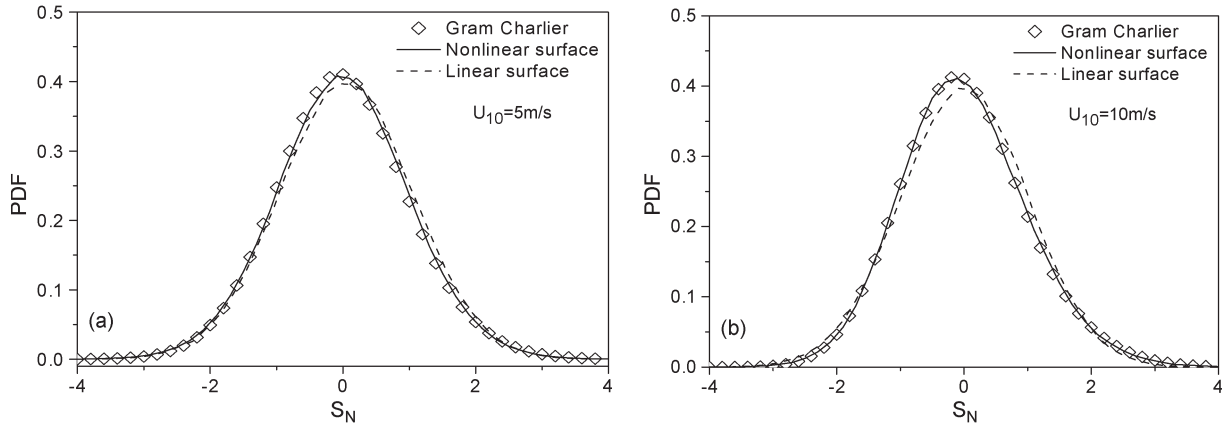


Fig. 3. Comparisons of the surface slope pdfs with the Gram–Charlier distribution.

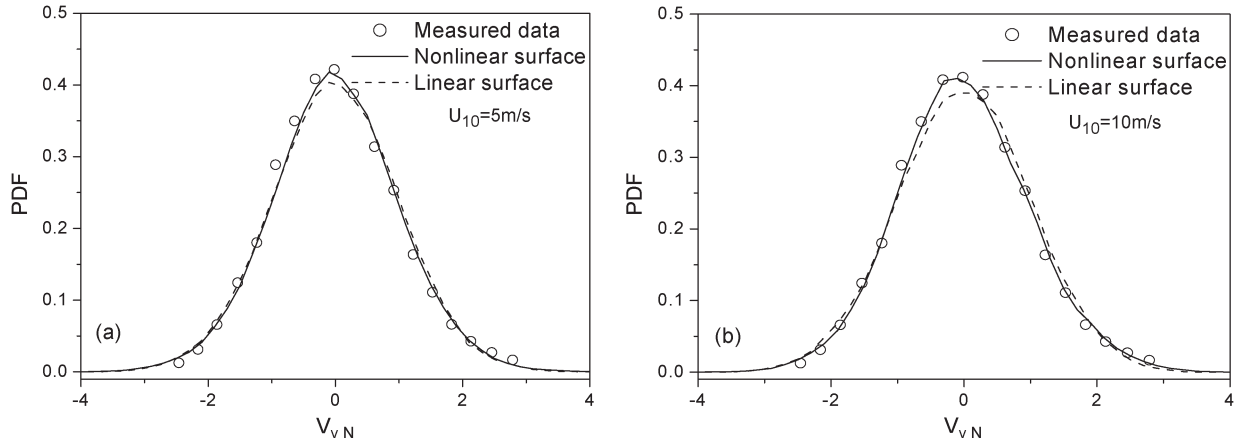


Fig. 4. PDF of normalized vertical component of orbit velocity corresponding to (solid line) nonlinear, (dashed line) linear, and (circles) measurements [44].

weighted by the scattering fields from bound waves should be larger. From Fig. 6, it is also found that, at large incidence angles, the Doppler spectra corresponding to the linear sea surface model are somewhat narrower than those simulated based on the nonlinear surface. From the comparisons between the Gaussian-shape spectra (red line) and the numerically simulated results (dark line), we can see that the Gaussian-shape curves fit the numerically simulated results well for the low-

wind-speed case. Nevertheless, when the wind speed equals to 16 m/s, the Gaussian-shape curves cannot fit the numerical simulations well at large incidence angles. Fig. 6 shows that the left-hand side of the simulated spectra is much steeper than that of Gaussian-shape curves. The reasons for this deviation are as follows: 1) The pdf of the orbit velocity of the LMLC surface cannot be described as a Gaussian distribution; 2) the Doppler spectrum is weighted by the scattering coefficient of

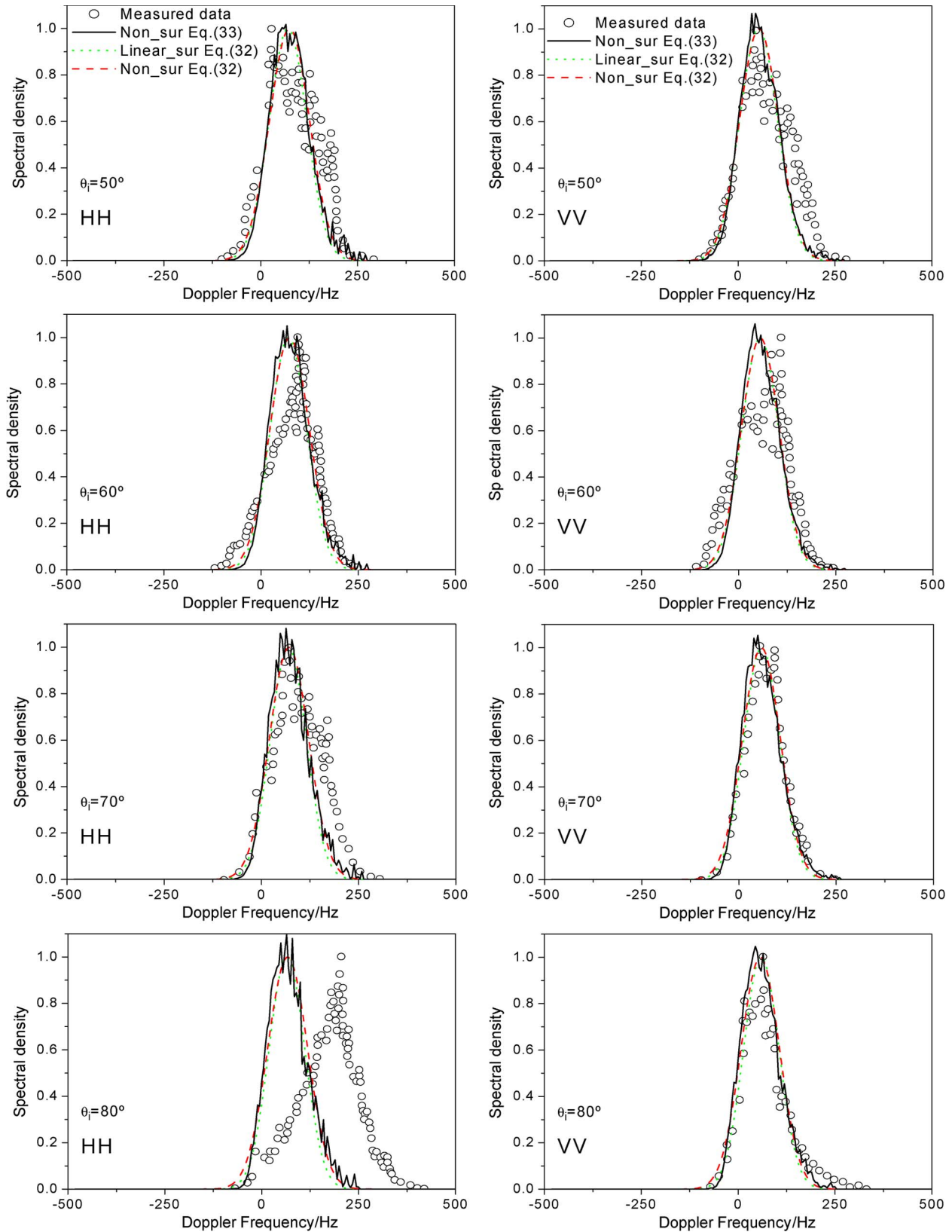


Fig. 5. Doppler spectra of signals backscattered from sea surface at $U_{47} = 7$ m/s wind speed for (left) HH and (right) VV polarization. (Circles) Experimental data [45]. (Dark line) Results simulated by (33) corresponding to nonlinear surface. (Red line) Results simulated by (32) corresponding to nonlinear surface. (Green line) Simulations of (32) corresponding to linear surface.

each surface facet, and thus, the modulation impacts the shape of the Doppler spectrum; and 3) the shadowing of large-scale waves also affects the spectral shape.

In Fig. 7, the Doppler shifts predicted by (29) are compared with the numerical simulations by Toporkov *et al.* [9], [46] at L-band (1.3 GHz) and X-band (10 GHz) radar frequencies with

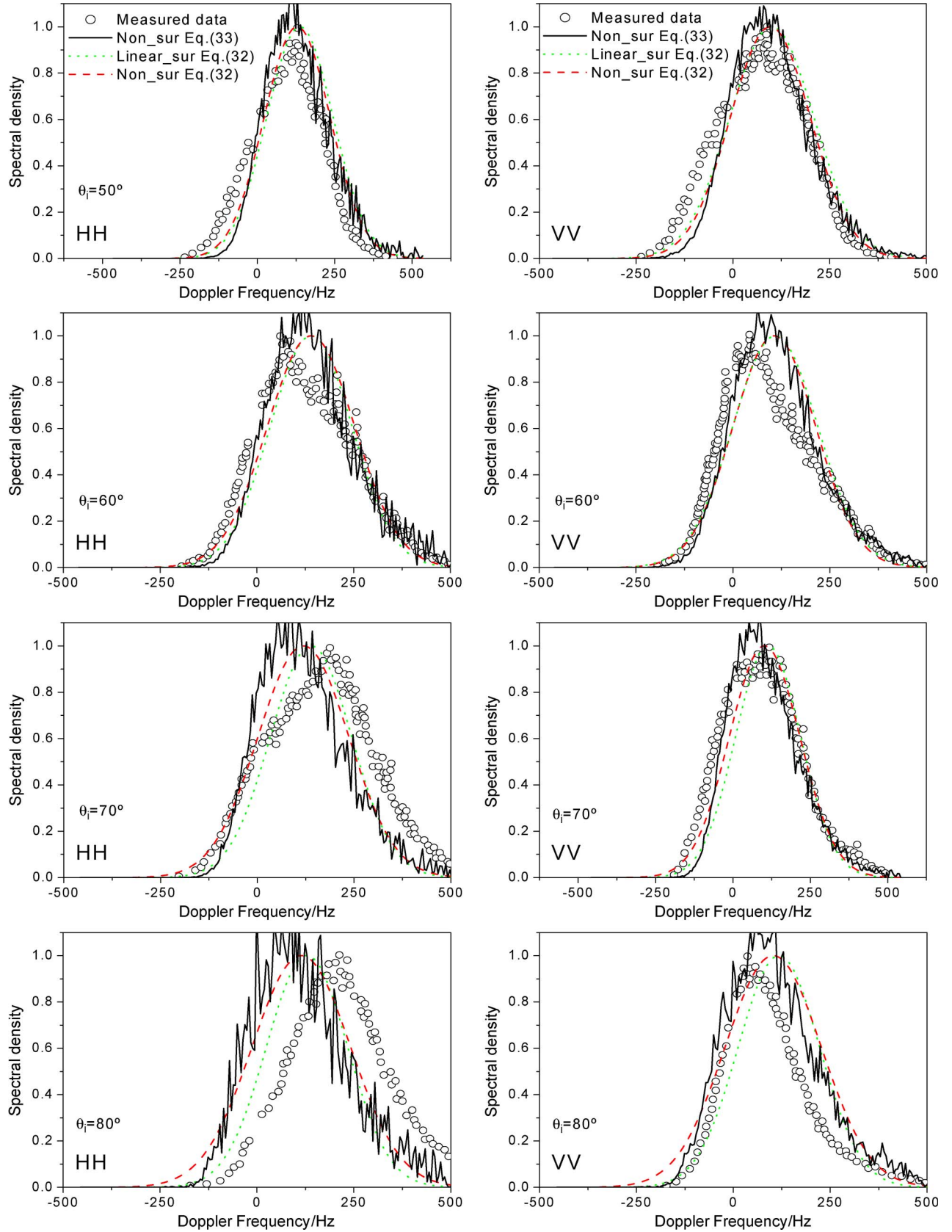


Fig. 6. Same as Fig. 5 but at a wind speed of $U_{47} = 16$ m/s.

different wind speeds at a height of 19.5 m above sea surface [in our simulations, $U_{19.5}$ has been recalibrated to U_{10} by (36)]. Here, we take the linking parameter $\alpha_i = 0$ in (5). In [9], the

mean Doppler spectra of backscattered fields from the nonlinear Creamer sea surface [20], [47], which is consistent with the LMLC model for the linking parameter $\alpha_i = 0$ in (5), were

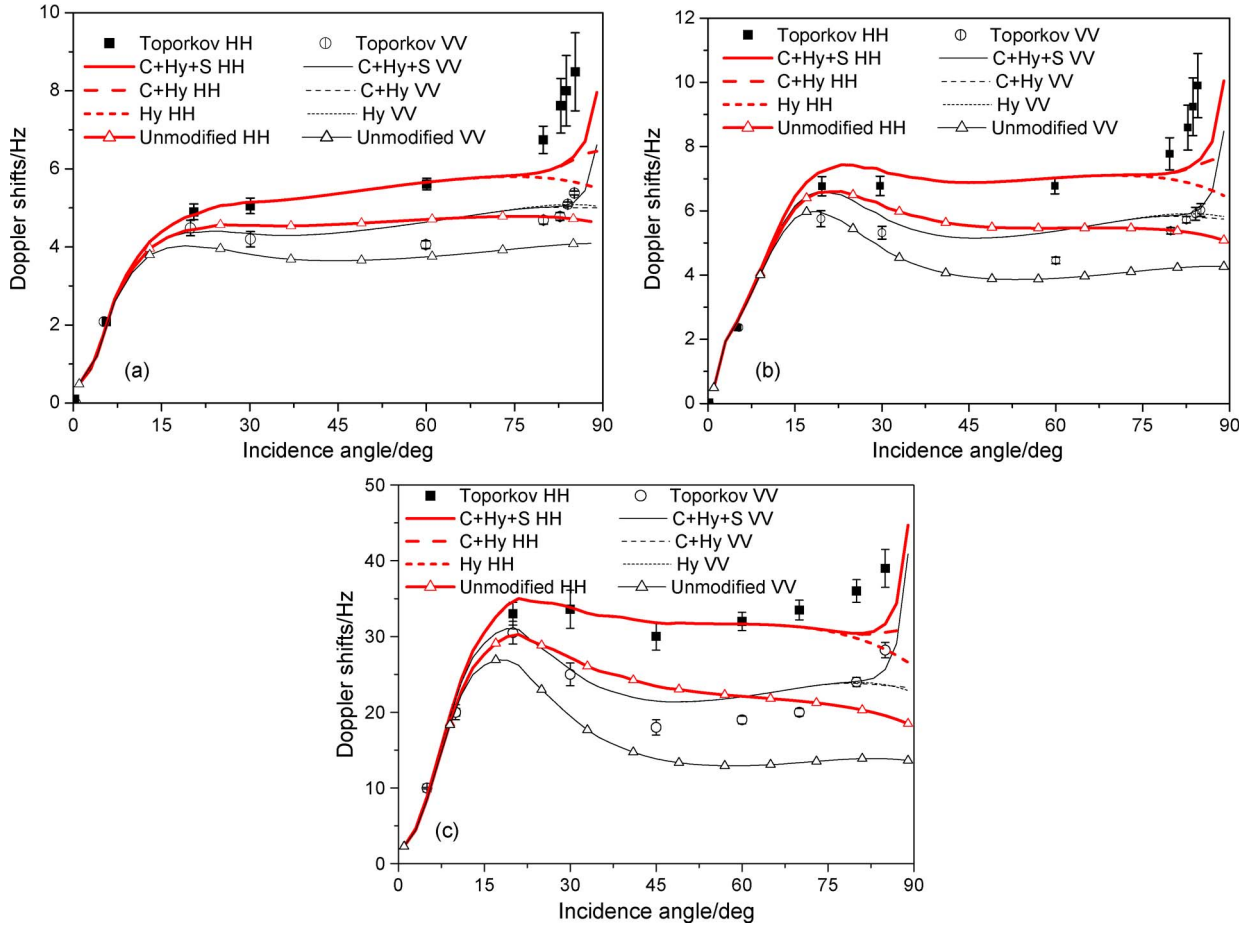


Fig. 7. Comparison of the Doppler shifts predicted by (29) and the numerical simulations by Toporkov *et al.* [9], [46]. (a) At L-band with wind speed $U_{19.5} = 5$ m/s. (b) At L-band with wind speed $U_{19.5} = 7$ m/s. (c) At X-band with wind speed $U_{19.5} = 5$ m/s. **C + Hy + S**: Influences of curvature, hydrodynamic modulation, and shadow are all considered. **C + Hy**: Influences of curvature and hydrodynamic modulation are considered. **Hy**: Only the influence of hydrodynamic modulation is considered. **Unmodified**: None of these modifications is considered. Vertical bars indicate $\pm 1\sigma$ statistical error.

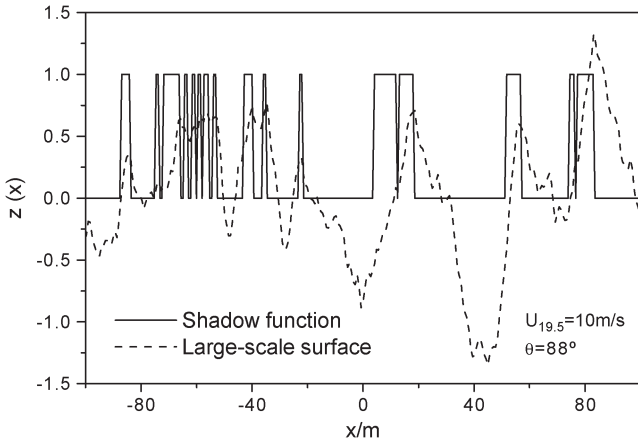


Fig. 8. Shadow of the large-scale wave.

simulated by the method of ordered multiple interactions. The first moment of the mean Doppler spectra, i.e., Doppler shift (or Doppler centroid), is defined as

$$f_{\text{dpp}} = \left| \frac{\int f S_{\text{mpp}}(f) df}{\int S_{\text{mpp}}(f) df} \right| \quad (37)$$

where $S_{\text{mpp}}(f)$ denotes the mean Doppler spectrum numerically simulated by Toporkov *et al.* As shown in Fig. 7, at

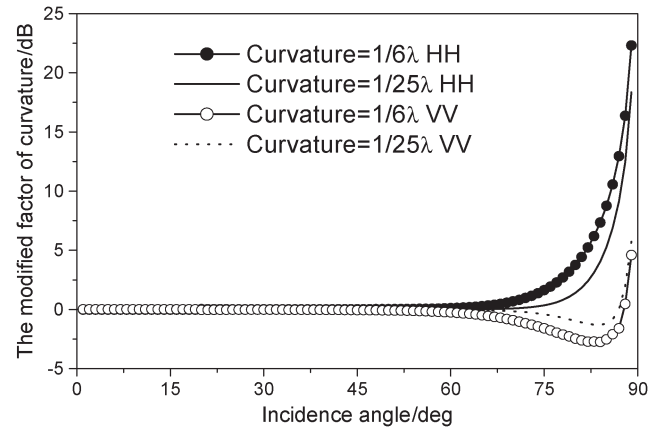


Fig. 9. Modified factor of curvature.

large incidence angles, the Doppler shift increases quickly if the influences of curvature and shadow are taken into account. This phenomenon is due to the following two reasons: 1) Results in Fig. 8 at large incidence angles show only some scattering facets in the vicinity of the crests which should be illuminated by the incident wave, and from (10), one can find that, near the crests, the horizontal component of the orbit velocity is large; and 2) Fig. 9 illustrates that the effect

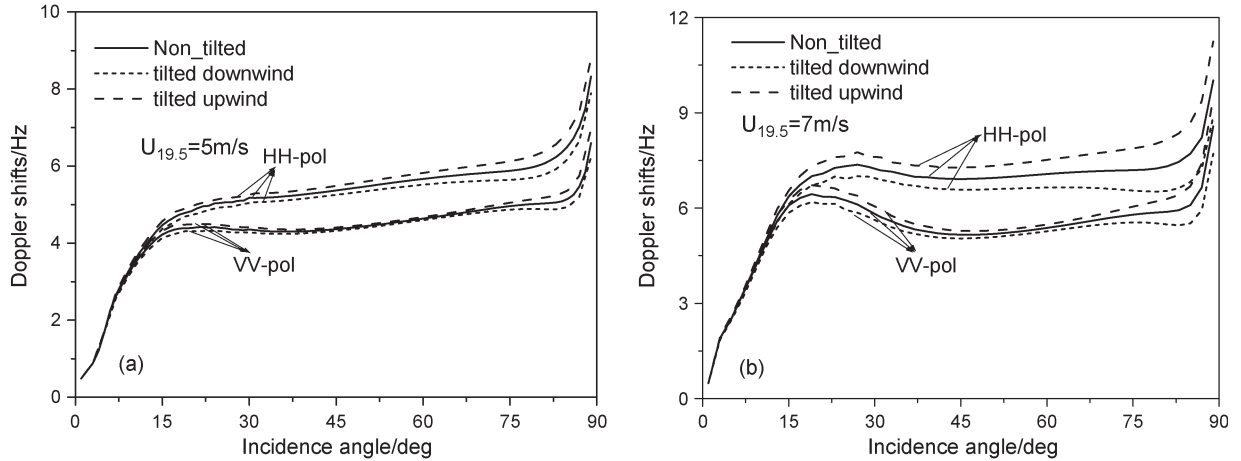


Fig. 10. Doppler shifts versus incident angle for the tilted and the nontilted sea surface. (a) Wind speed $U_{19.5} = 5$ m/s. (b) Wind speed $U_{19.5} = 7$ m/s.

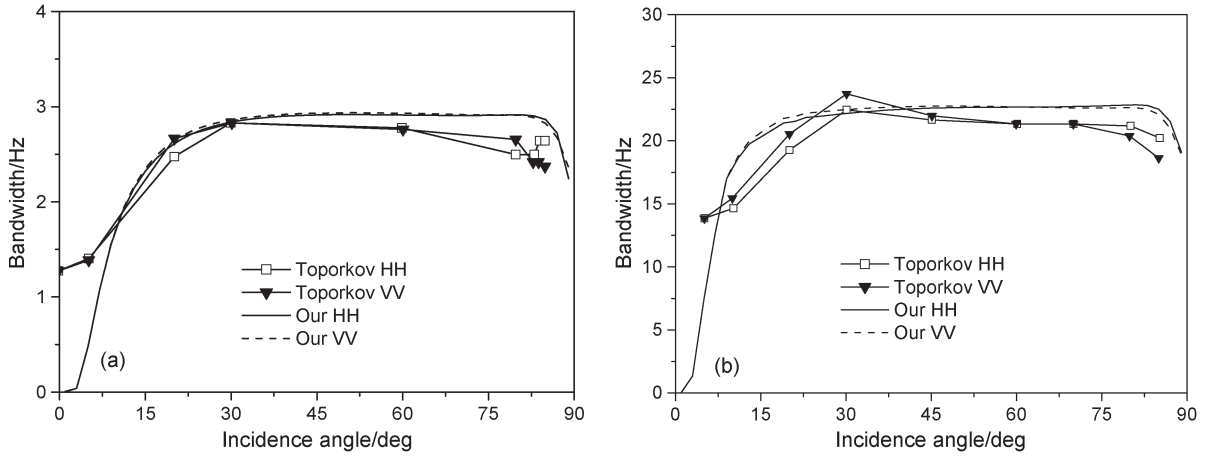


Fig. 11. Bandwidths of Doppler spectra for different radar frequencies. (a) L-band. (b) X-band.

of the curvature is very obvious, and the modified factor of curvature is greater with increasing curvature at LGAs. Because curvatures at wave peaks are larger, then, the total scattered field would be weighted significantly by the echoes backscattered from the region near wave peaks. From Fig. 7, one can also find that, for the VV-pol case, the influence of curvature on Doppler shift is insignificant. The reason is that the influence of curvature on VV-pol scattered fields is much less in contrast with HH-pol, just as shown in Fig. 9. Simulations in Fig. 7 also illustrate that hydrodynamic modulation induces remarkable influence on the predicted Doppler shifts. Meanwhile, we can also observe that the predicted Doppler shifts are always larger in HH polarization than in VV polarization due to the effect of the tilt modulation.

Fig. 10 illustrates a comparison between the Doppler shifts predicted from the tilted ($\gamma = 0.4$) and the nontilted ($\gamma = 0$) sea surface. Here, the radar frequency is 1.3 GHz. We can see that the Doppler shifts for the tilted surface predicted in the upwind direction are somewhat larger than those corresponding to the nontilted surface, while the Doppler shifts for the tilted surface are smaller in the downwind direction. Moreover, the horizontal skewness impacts the HH-pol results more obviously because the HH-pol scattering field is more sensitive to the sea surface slope. Meanwhile, it is also shown that the differences

between the results obtained in the upwind and the downwind direction increase with wind speed, and this is because the horizontal skewness of the sea surface becomes more significant as wind speed increases.

The bandwidths calculated by (31) are shown in Fig. 11 for different radar frequencies. Here, the wind speed is $U_{19.5} = 5$ m/s which has been recalibrated to U_{10} by (36), and the linking parameter $\alpha_i = 0$. Note that the bandwidth almost does not depend on polarization. At small incidence angles, it is found that the difference between our simulations and the numerical results by Toporkov *et al.* [46] is large. The reason for this difference is that, at small incidence angles, the Bragg scattering mechanism is invalid and, then, the bandwidth predicted by TSM is insufficient. Fig. 11 shows that the bandwidth is almost a constant at moderate incidence angles. However, at larger incidence angles, the bandwidth would decrease with the increase of the incidence angle due to the effect of shadow.

VI. CONCLUSION

On the basis of the composite surface scattering model, Doppler spectra of microwave signals from 1-D nonlinear sea surfaces have been simulated. Meanwhile, the dependences of the Doppler properties on the curvature, shadow, and

hydrodynamic modulation of large-scale waves are also discussed. From the comparisons between the simulated results and the measurements, we can find that the simulations based on nonlinear sea surfaces can fit the measured data better than those corresponding to the linear sea surface model. From what has been discussed in Section V, we can also obtain the conclusion that, at large incident angles, the Doppler shift increases more quickly with the incidence angle increasing due to the shadow and curvature effects of large-scale waves, but the bandwidth decreases with the incident angle.

Although this work is limited to 1-D nonlinear surface, conclusions obtained in this work will help to better understand time-dependent radar backscattered signal sensitivities to both sea surface characteristics and radar parameters. Further work should be carried out to investigate the properties of Doppler spectra from 2-D composite nonlinear sea surfaces.

ACKNOWLEDGMENT

The authors would like to thank the anonymous reviewers for providing valuable and constructive comments.

REFERENCES

- [1] D. D. Crombie, "Doppler spectrum of sea echo at 13.66 Mc/s.," *Nature*, vol. 175, pp. 681–682, 1955.
- [2] D. E. Barrick, "Extraction of wave parameters from measured HF radar sea-echo Doppler spectra," *Radio Sci.*, vol. 12, no. 3, pp. 415–424, 1977.
- [3] F. G. Bass, I. M. Fuks, A. I. Kalmykov, I. E. Ostrovsky, and A. D. Rosenberg, "Very-high frequency radio wave scattering by a disturbed sea surface, part II: Scattering from an actual sea surface," *IEEE Trans. Antennas Propag.*, vol. AP-16, no. 5, pp. 560–568, Sep. 1968.
- [4] J. W. Wright and W. C. Keller, "Doppler spectra in microwave scattering from wind waves," *Phys. Fluids*, vol. 14, no. 3, pp. 466–474, Mar. 1971.
- [5] V. U. Zavorotny and A. G. Voronovich, "Two-scale model and ocean radar Doppler spectra at moderate- and low-grazing angles," *IEEE Trans. Antennas Propag.*, vol. 46, no. 1, pp. 84–92, Jan. 1998.
- [6] B. J. Lipa, "Inversion of second-order radar echoes from the sea," *J. Geophys. Res.*, vol. 83, no. C2, pp. 959–962, 1978.
- [7] G. Soriano, M. Joelson, M. Saillard, and P. C. Marseille, "Doppler spectra from a two-dimensional ocean surface at L-band," *IEEE Trans. Geosci. Remote Sens.*, vol. 44, no. 9, pp. 2430–2437, Sep. 2006.
- [8] I. M. Fuks and A. G. Voronovich, "Radar backscattering from Gerstner's sea surface," *Waves Random Media*, vol. 12, no. 3, pp. 321–339, Jul. 2002.
- [9] J. V. Toporkov and G. S. Brown, "Numerical simulations of scattering from time-varying randomly rough surfaces," *IEEE Trans. Geosci. Remote Sens.*, vol. 38, no. 4, pp. 1616–1625, Jul. 2000.
- [10] J. T. Johnson, J. V. Toporkov, and G. S. Brown, "A numerical study of backscattering from time-evolving sea surfaces: Comparison of hydrodynamic models," *IEEE Trans. Geosci. Remote Sens.*, vol. 39, no. 11, pp. 2411–2420, Nov. 2001.
- [11] A. R. Hayslip, J. T. Johnson, and G. R. Baker, "Further numerical studies of backscattering from time-evolving nonlinear sea surfaces," *IEEE Trans. Geosci. Remote Sens.*, vol. 41, no. 10, pp. 2287–2293, Oct. 2003.
- [12] M. Saillard, P. Forget, G. Soriano, M. Joelson, P. Broche, and P. Carrier, "Sea surface probing with L-band Doppler radar: Experiment and theory," *C. R. Physique*, vol. 6, no. 6, pp. 675–682, Jul./Aug. 2005.
- [13] Y. Hisaki, "Doppler spectrum of radio wave scattering from ocean-like moving surfaces for finite illuminated area," *Int. J. Remote Sens.*, vol. 24, no. 15, pp. 3075–3091, 2003.
- [14] J. T. Johnson, R. J. Burkholder, J. V. Toporkov, D. R. Lyzenga, and W. J. Plant, "A numerical study of the retrieval of sea surface height profiles from low grazing angle radar data," *IEEE Trans. Geosci. Remote Sens.*, vol. 47, no. 6, pp. 1641–1650, Jun. 2009.
- [15] B. Chapron, F. Collard, and F. Ardhum, "Direct measurements of ocean surface velocity from space: Interpretation and validation," *J. Geophys. Res.*, vol. 110, p. C07008, 2005.
- [16] J. A. Johannessen, V. Kudryavtsev, D. Akimov, T. Eldevik, N. Winther, and B. Chapron, "On radar imaging of current features; part 2: Mesoscale eddy and current front detection," *J. Geophys. Res.*, vol. 110, p. C07017, 2005.
- [17] V. Kudryavtsev, D. Akimov, J. A. Johannessen, and B. Chapron, "On radar imaging of current features. Part 1: Model and comparison with observations," *J. Geophys. Res.*, vol. 110, p. C07016, 2005. doi:10.1029/2004JC002505.
- [18] A. Mouche, B. Chapron, N. Reul, and F. Collard, "Predicted Doppler shifts induced by ocean surface wave displacements using asymptotic electromagnetic wave scattering theories," *Waves Random Complex Media*, vol. 18, no. 1, pp. 185–196, 2008.
- [19] V. Karaev, M. Kanevsky, and E. Meshkov, "The effect of sea surface slicks on the Doppler spectrum width of a backscattered microwave signal," *Sensors*, vol. 8, no. 6, pp. 3780–3801, 2008.
- [20] D. B. Creamer, F. Henyey, R. Schult, and J. Wright, "Improved linear representation of ocean surface waves," *J. Fluid Mech.*, vol. 205, pp. 135–161, 1989.
- [21] G. Lindgren and S. Aberg, "First order stochastic Lagrange model for asymmetric ocean waves," *J. Offshore Mech. Arct. Eng.*, vol. 131, no. 3, p. 031602, Aug. 2009.
- [22] G. Lindgren, "Exact asymmetric slope distributions in stochastic Gauss-Lagrange ocean waves," *Appl. Ocean Res.*, vol. 31, no. 1, pp. 65–73, Feb. 2009.
- [23] W. C. Keller and J. W. Wright, "Microwave scattering and straining of wind generated waves," *Radio Sci.*, vol. 10, no. 2, pp. 139–147, 1975.
- [24] W. Alpers and K. Hasselmann, "The two-frequency microwave technique for measuring ocean-wave spectra from an airplane or satellite," *Boundary Layer Meteorol.*, vol. 13, pp. 215–230, 1978.
- [25] W. Alpers, D. B. Ross, and C. L. Rufenach, "On the detectability of ocean surface waves by real and synthetic aperture radar," *J. Geophys. Res.*, vol. 86, no. C7, pp. 6481–6498, Jul. 1981.
- [26] M. A. Tayfun, "On narrow-band representation of ocean waves 1. Theory," *J. Geophys. Res.*, vol. 91, no. C6, pp. 7743–7752, Jun. 1986.
- [27] A. K. Fung, *Microwave Scattering and Emission Models and Their Applications*. Boston, MA: Artech House, 1994.
- [28] K. S. Chen, A. K. Fung, and F. Amar, "An empirical bispectrum model for sea surface scattering," *IEEE Trans. Geosci. Remote Sens.*, vol. 31, no. 4, pp. 830–835, Jul. 1993.
- [29] T. Elfouhaily, B. Chapron, K. Katsaros, and D. Vandemark, "A unified directional spectrum for long and short wind-driven waves," *J. Geophys. Res.*, vol. 102, no. C7, pp. 15781–15796, 1997.
- [30] A. Masuda and Y. Y. Kuo, "A note on the imaginary part of bispectra," *Deep-Sea Res.*, vol. 28, no. 3, pp. 213–222, Mar. 1981.
- [31] S. Elgar and R. T. Guza, "Observation of bispectra of shoaling surface gravity waves," *J. Fluid Mech.*, vol. 161, pp. 425–448, 1985.
- [32] I. A. Leykin, M. A. Donelan, R. H. Mellen, and D. J. McLaughlin, "Asymmetry of wind waves studied in a laboratory tank," *Nonlinear Process. Geophys.*, vol. 2, no. 3/4, pp. 280–289, 1995.
- [33] M. S. Longuet-Higgins, "On the skewness of sea-surface slopes," *J. Phys. Oceanogr.*, vol. 12, no. 11, pp. 1283–1291, Nov. 1982.
- [34] E. A. Caponi, D. R. Crawford, H. C. Yuen, and P. G. Saffman, "Modulation of radar backscatter from the ocean by a variable current," *J. Geophys. Res.*, vol. 93, pp. 12249–12263, 1988.
- [35] A. G. Voronovich and V. U. Zavorotny, "Curvature effects in the composite model for low-grazing-angle rough-surface scatter," *Waves Random Media*, vol. 8, no. 1, pp. 41–52, 1998.
- [36] F. T. Ulaby, R. K. Moore, and A. K. Fung, *Microwave Remote Sensing*, vol. II. Reading, MA: Addison-Wesley, 1982.
- [37] A. G. Voronovich, "On the theory of electromagnetic waves scattering from the sea surface at low grazing angles," *Radio Sci.*, vol. 31, no. 6, pp. 1519–1530, 1996.
- [38] D. B. Trizna, "A model for Doppler peak spectral shift for low grazing angle sea scatter," *IEEE J. Ocean. Eng.*, vol. OE-10, no. 4, pp. 368–375, Oct. 1985.
- [39] W. C. Keller and W. J. Plant, "Microwave backscatter from the sea: Modulation of received power and Doppler bandwidth by long waves," *J. Geophys. Res.*, vol. 99, no. C5, pp. 9751–9766, 1994.
- [40] R. Romeiser and D. R. Thompson, "Numerical study on the along-track interferometric radar imaging mechanism of oceanic surface currents," *IEEE Trans. Geosci. Remote Sens.*, vol. 38, no. 1, pp. 446–458, Jan. 2000.
- [41] N. E. Huang and S. R. Long, "An experimental study of the surface elevation probability distribution and statistics of wind-generated waves," *J. Fluid Mech.*, vol. 101, pp. 179–200, 1980.
- [42] C. S. Cox and W. H. Munk, "Measurement of the roughness of the sea surface from photographs of the sun's glitter," *J. Opt. Soc. Amer.*, vol. 44, no. 11, pp. 838–850, Nov. 1954.

- [43] C. S. Cox and W. H. Munk, "Statistics of the sea surface derived from sun glitter," *J. Mar. Res.*, vol. 13, no. 2, pp. 198–227, 1954.
- [44] T. Honda and H. Mitsuyasu, "The statistical distributions for the elevation, velocity and acceleration of the surface of wind waves," *J. Oceanogr. Soc. Jpn.*, vol. 31, no. 2, pp. 93–104, Apr. 1975.
- [45] W. J. Plant, "A model for microwave Doppler sea return at high incidence angles: Bragg scattering from bound, tilted waves," *J. Geophys. Res.*, vol. 102, no. C9, pp. 21 131–21 146, 1997.
- [46] J. V. Toporkov, M. A. Sletten, and G. S. Brown, "Numerical scattering simulations from time-varying ocean-like surfaces at L- and X-band: Doppler analysis and comparisons with a composite surface analytical model," in *Proc. XXVII Gen. Assem. URSI*, Maastricht, The Netherlands, Aug. 17–24, 2002.
- [47] C. L. Rino, T. L. Crystal, A. K. Koide, H. D. Ngo, and H. Guthart, "Numerical simulation of backscatter from linear and nonlinear ocean surface realizations," *Radio Sci.*, vol. 26, no. 1, pp. 51–71, 1991.
- [48] H. A. Panofsky and J. A. Dutton, *Atmospheric Turbulence*. New York: Wiley, 1984.



Yunhua Wang was born in Shandong, China, in 1978. He received the M.S. and Ph.D. degrees in radio science from Xidian University, Xi'an, China, in 2005 and 2006, respectively.

He is currently an Associate Professor with the Ocean Remote Sensing Institute, Ocean University of China, Qingdao, China. His research interests include asymptotic and numerical simulations of electromagnetic wave scattering from random sea surfaces and synthetic-aperture-radar remote sensing of ocean.



Yanmin Zhang was born in Shandong, China, in 1979. She received the Ph.D. degree in optics from Huazhong University of Science and Technology, Wuhan, China, in 2007.

She is currently with the College of Information Science and Engineering, Ocean University of China, Qingdao, China. Her research interests include electromagnetic scattering from sea surface and applications for remote sensing.

Mingxia He was born in Shanghai City, China, on September 11, 1939. She is currently with the Ocean Remote Sensing Institute, Ocean University of China, Qingdao, China. Her research interests include optical and microwave remote sensing of ocean.

Chaofang Zhao was born in Shandong, China, in 1965. He is currently a Professor with the Ocean Remote Sensing Institute, Ocean University of China, Qingdao, China. His research interests are in the areas of microwave remote sensing and Lidar exploration of ocean.